I denote the external, excitatory, and inhibitory populations, respectively. Inhomogeneities are modeled by distributing the thresholds of population k uniformly between a minimum of $\theta_k\sqrt{K}$ and a maximum of $(\theta_k + D)\sqrt{K}$.

8. The total instantaneous input to a single neuron of population k = E, I consists of weakly correlated fluctuating contributions. Therefore, we can assume, for large K, that it has Gaussian statistics with a mean given by

$$u_k(t) = K \sum_{\ell=0,E,I} J_{k\ell} m_\ell(t) \quad (1)$$

and variance

$$\sigma_k^2(t) = K \sum_{\ell=E,I} (J_{k\ell})^2 m_\ell(t) \quad (2)$$

The variable $0 \leq m_\ell(t) \leq 1$ denotes the unit activities averaged over all the units in the ℓth population. It represents the firing rate of the neuronal population relative to its maximal rate. A detailed analysis also yields the short-time correlations of the input, which decay on a time scale of order unity. The external input does not contribute to the fluctuations.

9. To ensure that the saturated states (m_ℓ = 1 or 0) are not stable, the connection parameters $J_{k\ell}$ must obey certain easily satisfied inequalities. They also ensure the existence of a balanced state. The stationary balanced state is stable provided that the inhibitory time constant τ is smaller than an upper bound τ_c. The value of τ_c typically ranges from 0.5 to 1.5.
10. In the balanced state, the means u_k (Eq. 1) are roughly equal to the population-averaged thresholds $\theta_k\sqrt{K}$, yielding for population activities m_E and m_I the following linear relation to the external activity m_0

$$m_k = -\sum_{\ell=E,I} \mathbf{J}_{k\ell}^{-1}(J_{\ell 0} m_0 - K^{-1/2}\theta_\ell) \quad (3)$$

Here $\mathbf{J}^{-1}$ is the inverse of the 2 × 2 matrix of connections $J_{k\ell}$ between the two network populations. The activities are thresholded to zero when the above relations yield negative values.

11. M. Abeles, H. Bergman, E. Vaadia, unpublished data.
12. For comparison we consider a fully connected network of linear neurons where the coupling strengths between neurons in the network are equal to $J_{k\ell}/K$. These neurons integrate linearly their input with the same time constants as in the balanced network. The strengths of the synapses from cells outside of the network as well as the thresholds were chosen so that the stationary population rates of this network are the same as those for the balanced network.
13. H. Sompolinsky, A. Crisanti, H. J. Sommers, *Phys. Rev. Lett.* **61**, 259 (1988).
14. B. Derrida, E. Gardner, A. Zippelius, *Europhys. Lett.* **4**, 167 (1987). In this model, the randomness in the sign of the interactions is the result of the random nature of the embedded memories.
15. D. Hansel and H. Sompolinsky, *Phys. Rev. Lett.* **68**, 718 (1992); *J. Comput. Neurosci.* **3**, 5 (1996); P. C. Bush and R. J. Douglas, *Neural Comput.* **3**, 19 (1991).
16. We thank D. J. Amit, D. Hansel, and T. Sejnowski for extensive discussions. We are grateful to M. Abeles, H. Bergman, and E. Vaadia for permission to present their data.

11 June 1996; accepted 11 October 1996

Photolysis of the Carbon Monoxide Complex of Myoglobin: Nanosecond Time-Resolved Crystallography

Vukica Šrajer, Tsu-yi Teng, Thomas Ursby, Claude Pradervand, Zhong Ren, Shin-ichi Adachi, Wilfried Schildkamp, Dominique Bourgeois, Michael Wulff, Keith Moffat*

The biological activity of macromolecules is accompanied by rapid structural changes. The photosensitivity of the carbon monoxide complex of myoglobin was used at the European Synchrotron Radiation Facility to obtain pulsed, Laue x-ray diffraction data with nanosecond time resolution during the process of heme and protein relaxation after carbon monoxide photodissociation and during rebinding. These time-resolved experiments reveal the structures of myoglobin photoproducts, provide a structural foundation to spectroscopic results and molecular dynamics calculations, and demonstrate that time-resolved macromolecular crystallography can elucidate the structural bases of biochemical mechanisms on the nanosecond time scale.

Structural intermediates in biological reactions can be very short-lived, with lifetimes spanning the time scale from femtoseconds (*1*) to milliseconds or longer (*2*). Structural studies of these intermediates have been carried out either (i) by artificially prolonging the lifetime of intermediates by chemical or physical manipulations (*3–6*) or (ii) by developing very fast x-ray Laue techniques (*7*) for structure determination and applying them to authentic, short-lived intermediates. We describe a Laue crystallographic investigation with nanosecond time resolution of the structural changes that occur in the carbon monoxide complex of myoglobin (MbCO) at room temperature on CO photodissociation by a nanosecond laser pulse. The results reveal directly the structural relaxation of the heme and protein in response to the ligand photodissociation and rebinding. The MbCO photolysis reaction has been studied in solution by numerous spectroscopic techniques (*8–18*) and computational approaches by molecular dynamics simulations (*19–21*), to which we relate our crystallographic results.

The nanosecond time-resolved crystallographic data were collected at the white beam station BL3 (ID9) at the European Synchrotron Radiation Facility (ESRF), Grenoble, France. Photolysis was initiated by 7.5-ns laser pulses, and subsequent structural changes were monitored with either a single 150-ps x-ray pulse or a 940-ns pulse train (*22, 23*). Photolysis and CO rebinding were also monitored optically (*22*). Complete x-ray data sets were obtained (Table 1) to 1.8 Å resolution at six time delays between laser and x-ray pulses: 4 ns (150-ps x-ray exposure, 15-mA beam current, single-bunch mode of operation of ESRF), 1 μs, 7.5 μs, 50.5 μs, 350 μs, and 1.9 ms (940-ns x-ray exposure, 150 mA, one-third filling mode).

Difference Fourier maps corresponding to each of the six time delays (Fig. 1, A to F) reveal the differences between the average structure at a time delay t, Mb*(t), with the stable MbCO structure. The MbCO content of the Mb*(t) state, which results from either incomplete initial photolysis or ligand recombination, cancels out in these maps. The reference map (Fig. 1G) displays the difference in electron density between the conventional, static structures of deoxy Mb (*24*) and MbCO (*25*). With the exception of the maps at time delays of 350 μs and 1.9 ms, all show a prominent negative feature (labeled P in Fig. 1, A to D and G) corresponding to loss of the CO upon photolysis. The peak value of this feature at the 4-ns time delay corresponds to −9.8 σ where σ is the root-mean-square value of the difference electron density in the asymmetric unit. The magnitude of this feature declines with time as photodissociated CO recombines and, as expected, parallels the extent of recombination estimated from the time course of the optical signal (Fig. 2). That is, this feature carries information about ligand rebinding kinetics. The absence of features at longer time delays is also expected since optical data show that recombination of the photodissociated CO is complete by about 100 μs (Fig. 2). The longer time delay data therefore serve as negative controls to illustrate the complete optical and structural reversibility of the reaction. The initial fraction of photolyzed molecules is estimated to be 45 ± 10% from the initial amplitude of the optical change (*22*) and 42 ± 10% from comparison of the

V. Šrajer, T.-y. Teng, C. Pradervand, Z. Ren, W. Schildkamp, K. Moffat, Department of Biochemistry and Molecular Biology and the Consortium for Advanced Radiation Sources, The University of Chicago, Chicago, IL 60637, USA.
T. Ursby and M. Wulff, European Synchrotron Radiation Facility (ESRF), 38043 Grenoble Cedex, France.
S.-i. Adachi, Biophysical Chemistry Laboratory, Institute of Physical and Chemical Research, Saitama 351-01, Japan.
D. Bourgeois, UPR 9015/IBS, 38027 Grenoble, France, and ESRF, 38043 Grenoble Cedex, France.
*To whom correspondence should be addressed.

integrated electron contents of the negative, CO-associated feature A in Fig. 1, A and G. These results suggest that CO recombination in the crystal contains a fast, geminate phase having a recombination rate comparable with or greater than the maximum photolysis rate applied by the laser pulse of 10^9 s^{-1}, and confirm the qualitative observation by us and others (*26*) that it is much more difficult to photolyze MbCO molecules in this crystal form than in solution.

A second prominent, positive feature in the difference maps (labeled Q) is located on the bond between the iron and the proximal histidine, His^{93}; its largest magnitude is also found in the 4-ns map (Fig. 1A), with a peak value of plus 3.9 σ. This feature arises from the motion of the iron atom out of the heme plane toward the proximal histidine. The ratio of the integrated electron content of the CO-associated and Fe-associated features in the reference map (Fig. 1G) is 2.3, close to time-independent, experimental value of this ratio (Fig. 1, A to D) of 2.1. The decrease in electron content of both the Fe-associated and CO-associated features parallels CO recombination (Fig. 2) and the displacement of the iron is therefore effectively simultaneous with the loss of the CO, occurring in less than a few nanoseconds. Further, the full iron displacement of 0.32 Å from the heme plane (*24*, *25*) occurred in the photolyzed molecules. If displacement of the iron were slower or of lesser extent, the magnitude of the Fe-associated feature Q would be lower and it would apparently lag behind the CO-associated feature P and the optical data (Fig. 2), contrary to observation.

Several other features appear consistently above ±3σ in the experimental difference maps at locations identical to those of features in the reference map. The positive feature in the heme pocket in the 4-ns difference map (labeled R in Fig. 1A) may represent a transient "docking site" for the photodissociated CO, observed also by time-resolved infrared polarization spectroscopy (*10*). This feature has an integrated electron content of 1.8 e and its peak is located 1.2 Å from the photodissociated CO at 40 K (*5*) and 1.6 Å from the water molecule (labeled W in Fig. 1G) in the deoxy Mb heme pocket (*24*), surrounded by residues Ile^{107}, Val^{68}, and Leu^{29}. We do not identify any docking sites that might represent well-populated locations for the CO on other possible exit pathways. A positive feature (labeled S) in the vicinity of the distal histidine, His^{64}, coincides with a positive feature in the reference map (Fig. 1G) and is attributed to displacement of the distal histidine upon photolysis, toward the site formerly occupied by ligand. This feature is present above 3σ

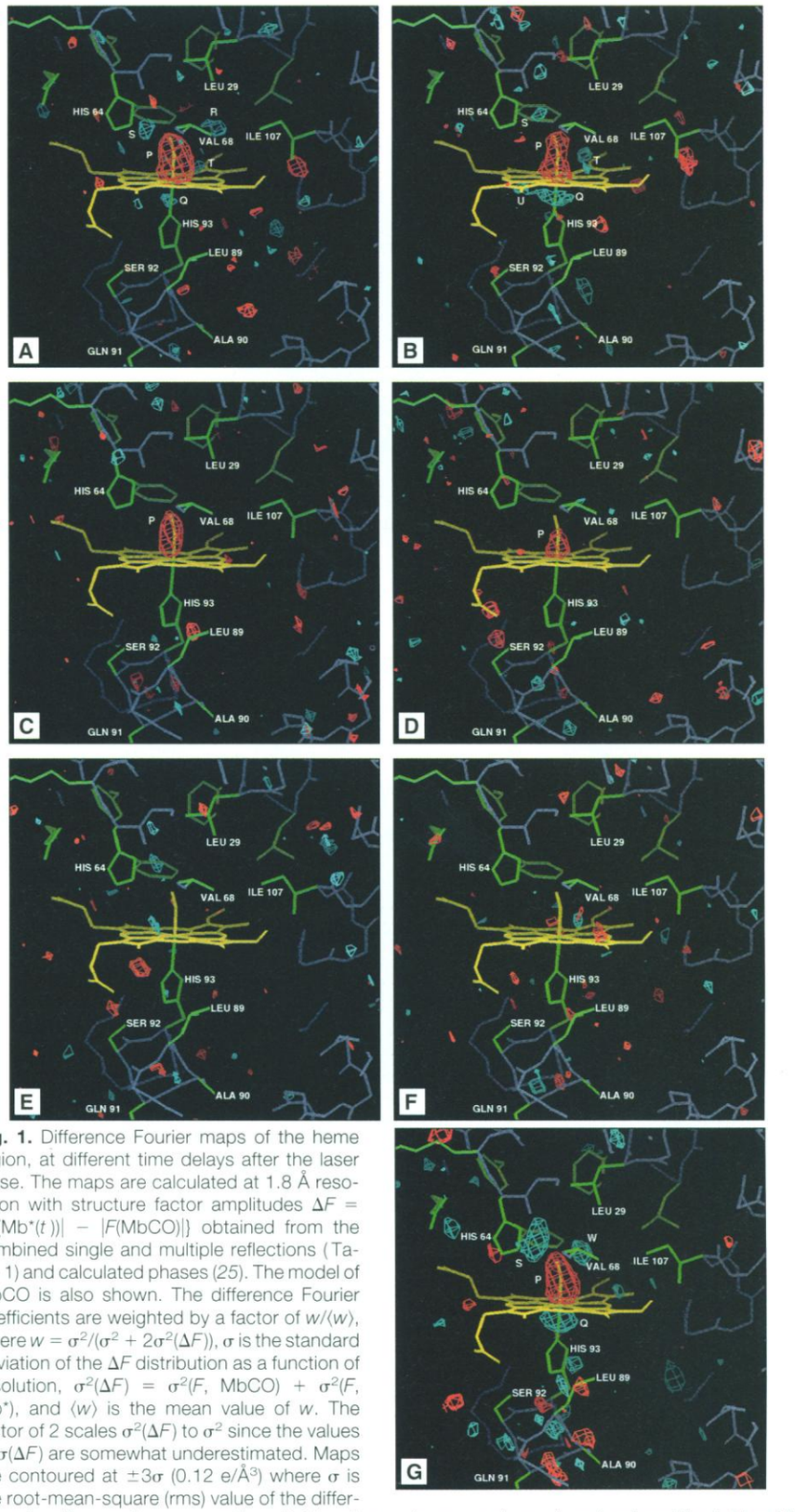

Fig. 1. Difference Fourier maps of the heme region, at different time delays after the laser pulse. The maps are calculated at 1.8 Å resolution with structure factor amplitudes $\Delta F = \{|F(\mathrm{Mb}^*(t))| - |F(\mathrm{MbCO})|\}$ obtained from the combined single and multiple reflections (Table 1) and calculated phases (*25*). The model of MbCO is also shown. The difference Fourier coefficients are weighted by a factor of $w/\langle w \rangle$, where $w = \sigma^2/(\sigma^2 + 2\sigma^2(\Delta F))$, σ is the standard deviation of the ΔF distribution as a function of resolution, $\sigma^2(\Delta F) = \sigma^2(F, \mathrm{MbCO}) + \sigma^2(F, \mathrm{Mb}^*)$, and $\langle w \rangle$ is the mean value of w. The factor of 2 scales $\sigma^2(\Delta F)$ to σ^2 since the values of $\sigma(\Delta F)$ are somewhat underestimated. Maps are contoured at ±3σ (0.12 e/Å^3) where σ is the root-mean-square (rms) value of the difference density over the asymmetric unit. Negative contours are shown in red and positive in blue. (**A**) Four-nanosecond time delay after CO photodissociation; (**B**) 1-μs delay; (**C**) 7.5-μs delay; (**D**) 50.5-μs delay; (**E**) 350-μs delay; (**F**) 1.9-ms delay; (**G**) the corresponding, reference difference Fourier map calculated from deoxy Mb (*24*) and MbCO (*25*) models with reflections identical to those in the 4-ns time delay x-ray data.

in both the 4-ns and 1-μs maps (Fig. 1, A and B). Another positive feature above the pyrrole-3 ring of the porphyrin (labeled T), present at 4 ns and 1 μs, together with the positive feature below the porphyrin ring (labeled U) present at 1 μs might arise from doming and slight rotation of the heme.

A number of smaller electron density features are present above ±3σ that indicate structural rearrangements of the residues surrounding the heme and in particular, the residues of the E and F helices spanning Lys[62] to Val[68] and Leu[89] to His[97], respectively. These features are consistent with the clearer differences in the reference map (Fig. 1G). Several of these features are already present at 4 ns, which indicates that some globin relaxation is closely associated in time with iron displacement and heme relaxation. Most of these features, however, seem more prominent at longer time delays, which suggests that globin relaxation is a complex process and continues to evolve over several decades in time, from ≤4 ns to at least 1 μs. Since these features associated with smaller tertiary structural changes lie close to the noise level we have not attempted at this stage to quantify structural changes by refining the Mb*(*t*) structures.

Our data support spectroscopic observations (*12*, *18*) and prediction by molecular dynamics simulation (*21*) of a fast, subnanosecond dissipation of vibrational energy after the large, transient increase in heme temperature on absorption of a visible photon. The transient photoproduct state at 4 ns shows no increase in the overall crystallographic temperature factor as compared to the initial MbCO state. The data also suggest that complete iron displacement and heme relaxation occur in ≤4 ns after CO photodissociation, in agreement with spectroscopic observations (*8*, *12*, *15*) and molecular dynamics simulations (*19*). Structural relaxation of the distal pocket residues and the F helix is stretched over several orders of magnitude in time as suggested by spectroscopic results (*13*, *14*) but appears to extend over a longer period, to the microsecond time domain. The plausible docking site of the photodissociated CO molecule is occupied at 4 ns (Fig. 1A) but not at 1 μs (Fig. 1B), in agreement with the time-resolved infrared measurements that estimate the lifetime of the CO trapped in a heme pocket site to be hundreds of nanoseconds (*10*). However, the occupancy of this docking site in the crystal is low; only about 40% of photodissociated CO molecules are present in this site at 4 ns. This observation is consistent with molecular dynamics simulations that suggest multiple pathways for escape of the CO molecule from the heme pocket (*20*).

The time courses of our structural and optical measurements on crystals do differ from those of spectroscopic measurements on solutions in one major point: a very rapid geminate CO rebinding process is considerably more prominent in crystals than in solution. This might result from real differences in structural relaxation processes of globin in the crystal and solution, in which the relaxation rates are slowed in the crystal because of constraints imposed by the intermolecular contacts in the crystal lattice, as they are in a viscous solution (*9*,

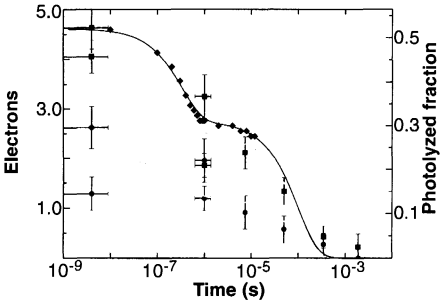

Fig. 2. Time course of the x-ray and optical signals. The electron content of the prominent CO-associated feature (P in Fig. 1, denoted by squares) and the Fe-associated feature (Q in Fig. 1, denoted by circles) is shown as a function of time. The vertical error bars are calculated from the mean value of the electron content of the same volume at random locations in the unit cell. The horizontal error bars indicate the time range over which data were averaged. The CO rebinding process measured optically (denoted by diamonds) consists of two phases fit by a sum of two exponentials (solid black line) with amplitudes (in units of photolyzed fraction) of 0.21 and 0.31 and rates of $3 \cdot 10^6$ s^{-1} and 10^4 s^{-1}. The gray lines that trace the electron content of CO and Fe features are fits by the same two exponential process, with scaling factors of 8.0 e for the CO feature and 3.9 e for the Fe feature. If the second phase is identified with the bimolecular recombination reaction, a second-order association rate constant of $2.5 \cdot 10^6$ M^{-1} s^{-1} is obtained, compared to the value of $0.5 \cdot 10^6$ M^{-1} s^{-1} in solution (*17*).

Table 1. Crystallographic data collection and reduction. Diffraction data were collected as described (*23*). Six pairs of data sets were collected at 19.4° ± 0.1°C. Each pair consists of an MbCO data set taken immediately before and an Mb* data set taken at a specific time delay after the laser exposure. Consecutive x-ray exposures were separated by at least 15 s to allow for the complete recovery of the crystal (lattice and myoglobin molecules) to the initial state. A data set consisted of about 50 images, each repeated three times for the 150-ps exposures, 4° apart in φ, to cover the 180° range necessary. These complete, highly redundant data sets were collected in order to further maximize the weak signal. No significant x-ray radiation or laser damage was detected. Data were reduced with the use of the Laue View (*31*) software package, and distinguished those reflections stimulated by one energy (singles), several energies (multiples), or their combination.

Laser to x-ray pulse delay state†	MbCO	4 ns Mb*	1 μs Mb*	7.5 μs Mb*	50.5 μs Mb*	350 μs Mb*	1.9 ms Mb*
			Singles				
Observations‡	34,801	33,063	34,241	34,010	35,232	34,772	32,958
Unique reflections	7,289	7,160	7,292	7,118	7,535	7,236	7,070
Overall redundancy	4.8	4.6	4.7	4.8	4.7	4.8	4.7
R_{merge} on F^2 (%)§	10.3	10.2	8.6	11.4	10.1	9.2	11.8
R_{merge} on $\|F\|$ (%)‖	6.9	6.9	5.8	7.5	6.8	6.0	7.7
			Singles and multiples combined				
Unique reflections¶	8143	8032	8108	8058	8280	8057	7871
R_{MbCO/Mb^*} (%)#		8.6	7.3	10.2	8.3	6.6	9.6
Resolution range (Å)				Completeness (%)††			
∞–10.80		27.8(27.8)	26.1(26.1)	13.9(13.9)	22.6(22.6)	24.3(24.3)	13.9(13.9)	24.3(24.3)
10.80–5.40		85.5(78.0)	86.6(78.8)	78.9(70.6)	87.8(79.4)	87.7(79.5)	77.6(69.4)	86.4(78.3)
5.40–3.60		94.1(89.3)	93.7(89.3)	94.4(87.3)	95.0(90.3)	95.4(90.6)	93.6(86.3)	94.6(89.8)
3.60–2.41		92.3(91.4)	91.4(90.8)	93.1(91.3)	93.0(91.8)	93.9(92.9)	92.4(90.6)	92.3(91.5)
2.41–2.02		70.5(82.8)	68.9(81.8)	70.1(82.6)	69.6(82.7)	74.2(85.3)	69.9(82.1)	69.7(82.6)
2.02–1.80		27.8(66.7)	27.0(65.7)	27.0(66.3)	21.5(64.7)	23.6(67.1)	27.1(65.9)	20.0(64.2)

†State refers to data taken before (MbCO) or after (Mb*) the laser pulse. For all laser to x-ray pulse delays, both MbCO and Mb* data sets were collected. Since the quality of the MbCO and Mb* data is similar, as demonstrated for 4-ns delay, for longer time delays only statistics for Mb* are shown. ‡Observations with $I/\sigma(I) > 0.1$, where I is the intensity of an observed reflection from a profile fit and $\sigma(I)$ is the residual from the fit. All data were integrated to 1.8 Å resolution. §$R_{merge} = \Sigma |F^2 - \langle F^2 \rangle| / \Sigma F^2$, where F^2 is the square of the structure factor amplitude of an observed reflection, calculated by scaling the measured intensity by a general scale factor (*31*), and $\langle F^2 \rangle$ is the average F^2 from multiple observations. ‖$R_{merge} = \Sigma \| |F| - \langle |F| \rangle | / \Sigma |F|$, where $|F|$ is the structure factor amplitude and $\langle |F| \rangle$ is the average amplitude from multiple observations. ¶Unique reflections with $F/\sigma(F) > 2$, where σ_F is the rms deviation determined from merging of structure amplitudes. #$R_{MbCO/Mb^*} = \Sigma \| |F|_{MbCO} - S \cdot |F|_{Mb^*} | / \Sigma |F|_{MbCO}$, where $|F|_{MbCO}$ and $|F|_{Mb^*}$ are the observed structure factor amplitudes for MbCO and Mb*, respectively, and S is the scaling factor. ††Completeness by resolution shells for singles and multiples combined. Cumulative completeness is also shown in parentheses. Binning is based on d_{min} value (1.8 Å): $6d_{min}$, $3d_{min}$, and $2d_{min}$ for resolutions lower than $2d_{min}$. For resolution higher than $2d_{min}$, equal shell volume binning is used.

11, *13*) or at low temperatures (*11*, *16*). Hence, much of the photodissociated CO cannot escape from the ligand pocket in the 7.5-ns duration of the laser pulse and recombines in a geminate fashion. Further, even for those molecules in which the CO does escape from the ligand pocket, globin relaxation does not proceed fully to completion in the crystal before rebinding of CO occurs.

Our results show that nanosecond time-resolved macromolecular crystallography is indeed feasible and extend the time resolution of macromolecular crystallography by six orders of magnitude, from milliseconds (*27*) to nanoseconds. The time resolution can be extended to the 100-ps domain if shorter laser pulses are used. Purposeful experimental design and Laue data acquisition and reduction strategies (*22*, *23*) yield significant features in the resultant time-dependent difference electron density maps, even from the weak diffraction patterns resulting from x-ray exposure times of only 150 ps.

REFERENCES AND NOTES

1. J.-L. Martin and M. H. Vos, *Annu. Rev. Biophys. Biomol. Struct.* **21**, 199 (1992).
2. D. W. J. Cruickshank, J. R. Helliwell, L. N. Johnson, Eds., *Time-resolved Macromolecular Crystallography* (Oxford Science Publications, Oxford, UK, 1992); K. Moffat, *Annu. Rev. Biophys. Biophys. Chem.* **18**, 309 (1989).
3. J. M. Bolduc *et al.*, *Science* **268**, 1312 (1995).
4. S. Sikora, A. S. Little, T. G. Dewey, *Biochemistry* **33**, 4454 (1994).
5. T.-Y. Teng, V. Šrajer, K. Moffat, *Nature Struct. Biol.* **1**, 701 (1994). Coordinates from related studies by Schlichting *et al.*, *Nature* **317**, 808 (1994) and Hartmann *et al.*, *Proc. Natl. Acad. Sci. U.S.A.* **93**, 7013 (1996) are not yet available. The three studies differ in key experimental conditions.
6. K. Moffat and R. Henderson, *Curr. Opin. Struct. Biol.* **5**, 656 (1995).
7. K. Moffat, D. Szebenyi, D. Bilderback, *Science* **223**, 1423 (1984).
8. S. Franzen, B. Bohn, C. Poyart, J.-L. Martin, *Biochemistry* **34**, 1224 (1995).
9. S. J. Hagen, J. Hofrichter, W. A. Eaton, *Science* **269**, 959 (1995).
10. M. Lim, T. A. Jackson, P. A. Anfinrud, *ibid.*, p. 962; ———, *J. Chem. Phys.* **102**, 4355 (1995).
11. A. Ansari, C. Jones, E. R. Henry, J. Hofrichter, W. A. Eaton, *Biochemistry* **33**, 5128 (1994).
12. M. Lim, T. A. Jackson, P. A. Anfinrud, *Proc. Natl. Acad. Sci. U.S.A.* **90**, 5801 (1993).
13. A. Ansari, C. M. Jones, E. R. Henry, J. Hofrichter, W. A. Eaton, *Science* **256**, 1796 (1992).
14. W. D. Tian, J. T. Sage, V. Šrajer, P. M. Champion, *Phys. Rev. Lett.* **68**, 408 (1992); L. Genberg, L. Richard, G. McLendon, R. J. D. Miller, *Science* **251**, 1051 (1991); X. Xie and J. D. Simon, *Biochemistry* **30**, 3682 (1991).
15. S. M. Janes, G. A. Dalickas, W. A. Eaton, R. M. Hochstrasser, *Biophys. J.* **54**, 545 (1988).
16. R. H. Austin, K. W. Beeson, L. Eisenstein, H. Frauenfelder, I. C. Gunsalus, *Biochemistry* **14**, 5355 (1975).
17. Q. H. Gibson, J. S. Olson, R. E. McKinnie, R. J. Rohlfs, *J. Biol. Chem.* **261**, 10228 (1986).
18. P. Li, J. T. Sage, P. M. Champion, *J. Chem. Phys.* **97**, 3214 (1992); R. Lingle Jr. *et al.*, *J. Am. Chem. Soc.* **113**, 3992 (1991).
19. H. Li, R. Elber, J. E. Straub, *J. Biol. Chem.* **268**, 17908 (1993); K. Kuczera, J.-C. Lambry, J.-L. Martin, M. Karplus, *Proc. Natl. Acad. Sci. U.S.A.* **90**, 5805 (1993); O. Schaad, H.-X. Zhou, A. Szabo, W. A. Eaton, E. Henry, *ibid.*, p. 9547.
20. R. Elber and M. Karplus, *J. Am. Chem. Soc.* **112**, 9161 (1990).
21. E. R. Henry, W. A. Eaton, R. M. Hochstrasser, *Proc. Natl. Acad. Sci. U.S.A.* **83**, 8982 (1986).
22. Sperm whale met Mb was used to grow crystals in the monoclinic form at pH 6 (*28*), which were converted to the MbCO form as described (*5*). Crystals with typical dimensions of 0.4 mm by 0.3 mm by 0.07 mm contained <5% of met Mb. Optical monitoring (*29*) with relatively weak (50 mW/mm^2), polarized light at 543 nm was essential to determine the best conditions for crystal photolysis, and to examine both the extent of photolysis just before the actual x-ray data collection and the kinetics of ligand rebinding after photolysis. The crystals were photolyzed by unpolarized 7.5-ns pulses at 635 nm from a Nd:YAG pumped dye laser (Continuum NY61-10/ND60), with DCM 630 dye. At 635 nm the crystal absorbance A is ≤0.2, which ensures relatively uniform photolysis in the longitudinal direction and minimizes photochemical and thermal gradients (*30*). Absorbance changes ΔA of crystals were measured as a function of laser pulse energy density to determine appropriate conditions for maximum photolysis. We estimate that a relative absorbance change, $\Delta A/A$, of 0.25 at 543 nm would be observed on complete photolysis. The maximum value of $\Delta A/A$ before irreversible crystal damage occurred was 0.1 to 0.12, which corresponds to 40 to 50% photolysis, and was accomplished with a pulse energy of 13 mJ and an 0.75-mm diameter laser beam size at the crystal location. Only about 0.5 to 1 mJ of the pulse energy was actually absorbed by the crystals, because of their small cross-sectional area and low absorbance at this wavelength. This corresponds to a photolysis rate of about $10^9\ s^{-1}$, which in turn is equivalent to about five photons absorbed per pulse per molecule. If we assume that half of the absorbed laser pulse energy appears as heat (*16*), the maximum temperature jump in the crystal does not exceed 10 K.
23. D. Bourgeois *et al.*, *J. Synchrotron Rad.* **3**, 65 (1996).
24. S. E. V. Phillips, *Brookhaven Protein Data Bank* (1981), Identification Code 1MBD.
25. J. Kuriyan, S. Wilz, M. Karplus, G. A. Petsko, *J. Mol. Biol.* **192**, 133 (1986).
26. L. Zhu, J. T. Sage, A. A. Rigos, D. Morikis, P. M. Champion, *ibid.* **224**, 207 (1992); I. E. T. Iben, L. Keszthelyi, D. Ringe, G. Váró, *Biophys. J.* **56**, 459 (1989); D. Morikis, T. J. Sage, A. K. Rizos, P. M. Champion, *J. Am. Chem. Soc.* **110**, 6341 (1988).
27. U. Genick *et al.*, in preparation.
28. J. C. Kendrew and R. G. Parrish, *Proc. R. Soc. London Ser. A* **238**, 305 (1956).
29. Y. Chen, V. Šrajer, K. Ng, A. LeGrand, K. Moffat, *Rev. Scient. Instrum.* **65**, 1506 (1994).
30. K. Ng, E. D. Getzoff, K. Moffat, *Biochemistry* **34**, 879 (1995).
31. Z. Ren and K. Moffat, *J. Appl. Cryst.* **28**, 461 (1995); *ibid.*, p. 482.

32. We thank J.-L. Laclare and the accelerator physics staff of ESRF for assistance; M. Roth for the use of his pulsed laser and for assistance and discussions; S. Labouré, C. Rubin, and A. LeGrand for experimental assistance; and C.-I. Brändén for continued support. Supported by the W. M. Keck Foundation, NIH GM 36452 and RR 07707 (K.M.), and a grant-in-aid for Scientific Research on Priority Areas (06235102) from the Ministry of Education, Science, and Culture, Japan (S.-i.A.).

8 July 1996; accepted 15 October 1996

Survival of Cholinergic Forebrain Neurons in Developing p75^{NGFR}-Deficient Mice

Catharina E. E. M. Van der Zee, Gregory M. Ross, Richard J. Riopelle, Theo Hagg*

The functions of the low-affinity p75 nerve growth factor receptor (p75^{NGFR}) in the central nervous system were explored in vivo. In normal mice, approximately 25 percent of the cholinergic basal forebrain neurons did not express TrkA and died between postnatal day 6 and 15. This loss did not occur in p75^{NGFR}-deficient mice or in normal mice systemically injected with a p75^{NGFR}-inhibiting peptide. Control, but not p75^{NGFR}-deficient, mice also had fewer cholinergic striatal interneurons. Apparently, p75^{NGFR} mediates apoptosis of these developing neurons in the absence of TrkA, and modulation of p75^{NGFR} can promote neuronal survival. Cholinergic basal forebrain neurons are involved in learning and memory.

Nerve growth factor (NGF) acts primarily through activation of its specific high-affinity TrkA tyrosine kinase receptor (*1*, *2*). The p75^{NGFR} is the product of a different gene and can bind all NGF-related neurotrophins (*1*, *2*). The complete set of p75^{NGFR} functions remains to be elucidated, but may include (*1*, *2*) providing ligand-binding specificity for NGF, enhancement of TrkA function, and mediating retrograde transport of selected neurotrophins (*3*). The p75^{NGFR} has at least two TrkA-independent signaling capacities: by its induction of NF-κB (*4*) and activation of the sphingomyelin pathway (*5*). Activation of the sphingomyelin pathway and formation of ceramide (*5*) can initiate apoptosis (cell death) through the stress-associated protein kinase pathway (*6*). Ceramide can stimulate cell proliferation, differentiation, and survival (*7*) perhaps through its metabolite sphingosine-1-phosphate, which activates mitogenic pathways and inhibits ceramide (*8*). When p75^{NGFR} is overexpressed in im-

C. E. E. M. Van der Zee and T. Hagg, Department of Anatomy and Neurobiology, Tupper Building, Dalhousie University, Halifax, Nova Scotia B3H 4H7, Canada.
G. M. Ross and R. J. Riopelle, Department of Medicine (Neurology), Queen's University, Kingston, Ontario K7L 2V7, Canada.

*To whom correspondence should be addressed. E-mail: thagg@is.dal.ca